

Constructing Periodic Phase Space Orbits from *ab Initio* Molecular Dynamics Trajectories to Analyze Vibrational Spectra: Case Study of the Zundel (H_5O_2^+) Cation

Scott M. Dietrick and Srinivasan S. Iyengar*

Department of Chemistry and Department of Physics, Indiana University, Bloomington, Indiana 47405, United States

S Supporting Information

ABSTRACT: A method of analysis is introduced to probe the spectral features obtained from *ab initio* molecular dynamics simulations. Here, the instantaneous mass-weighted velocities are projected onto irreducible representations constructed from discrete time translation groups comprising operations that invoke the time-domain symmetries (or periodic phase space orbits) reflected in the spectra. The projected velocities are decomposed using singular value decomposition (SVD) to construct a set of “modes” pertaining to a given frequency domain. These modes now include all anharmonicities, as sampled during the dynamics simulations. In this approach, the underlying motions are probed in a manner invariant with respect to coordinate transformations, operations being performed along the time axis rather than coordinate axes, making the analysis independent of choice of reference frame. The method is used to probe the underlying motions responsible for the doublet at $\sim 1000\text{ cm}^{-1}$ in the vibrational spectrum of the H_5O_2^+ , Zundel cation. The associated analysis results are confirmed by projecting the Fourier transformed velocities onto the harmonic normal mode coordinates and a set of mass-weighted, symmetrized Jacobi coordinates. It is found that the two peaks of the doublet are described and differentiated by their respective contributions from the proton transfer, water–water stretch, and water wag coordinates, as these are defined. Temperature dependent effects are also briefly noted.

1. INTRODUCTION

In a recent series of publications, we used *ab initio* molecular dynamics (AIMD)^{1–9} and quantum wavepacket *ab initio* molecular dynamics (QWAIMD)^{10–13} to compute vibrational properties in hydrogen bonded clusters. While *ab initio* molecular dynamics allows the “on-the-fly” treatment of electronic structure with simultaneous classical dynamical treatment of nuclei, quantum wavepacket *ab initio* molecular dynamics, in addition, includes a quantum dynamical treatment of a subset of nuclei. The vibrational studies constructed thus far using these methods include (a) a detailed study of the dynamically averaged vibrational spectrum that appropriately models the experimental situation for the protonated 21-water cluster,^{5,6} (b) the evaluation of the solvation structure and dynamics in medium-sized hydroxide and other negative ion water clusters,^{3,14–16} (c) analysis of energy redistribution in radicals of significance in atmospheric chemistry,^{4,8,9,17} (d) treatment of anharmonically coupled hydrogen-bonded systems along with a detailed elucidation of multiple experimental situations that yield widely different H/D isotope dependent vibrational properties.^{1,2} In fact, as far as we are aware, the studies in refs 1 and 2 represent the first time that a high level of concordance has been achieved between the experiments, infrared multiple photon dissociation (IRMPD)^{18–24} and argon-tagged action spectroscopy,²⁵ and a single set of theoretical results, for a set of spectra of a hydrogen-bound system, incorporating both a wide temperature range and isotopic effects. In addition to the above, *ab initio* molecular dynamics has been used to predict the amphiphilic nature of the hydrated proton in medium to large sized protonated water clusters.^{6,7} In all cases mentioned above, the vibrational spectral

properties are constructed using correlation functions obtained from dynamical parameters. For example, for cases where nuclei are treated classically, constructs proportional to the dipole and velocity autocorrelation functions are employed, whereas for situations where the nuclei are treated quantum dynamically, as a wavepacket, a quantum-mechanical flux autocorrelation function is utilized.^{10,12}

The studies described above can be contrasted with other approaches commonly used in the literature. One of the most common methods is to obtain vibrational properties through harmonic analyses constructed at optimized nuclear configurations. Such approaches are now a standard part of most electronic structure packages. However, these approaches are not adequate for soft vibrational modes such as those encountered in hydrogen-bonded systems.^{1–3,5,6,10} The effect of the potential on the nuclei must be considered beyond the harmonic approximation through either explicit quantum-mechanical,^{26–37} semiclassical,^{30,38–48} or classical treatment of nuclei. When such treatments are combined with electronic structure calculations, either performed “on-the-fly” or *a priori*, one may be able to construct an accurate vibrational analysis. In addition, quantum nuclear effects may be included using a variety of methods.^{10,31,49–52} However, as seen, for example, in refs 10 and 49, the accurate treatment of hydrogen bonded systems that includes (a) anharmonicities sometimes at quartic or higher orders and (b) donor–acceptor fluctuations driven

Special Issue: Berny Schlegel Festschrift

Received: August 7, 2012

Published: October 2, 2012

and coupled to the double well-type potentials acting on the shared proton still presents a major challenge to most theoretical methods. As indicated in the references cited above, our previous AIMD and QWAIMD studies have been reasonably successful in the study of such systems and in some cases have provided fresh insight into experimental findings.^{1,2,5,6}

However, challenges remain in the treatment of vibrational properties, particularly in the area of spectral interpretation. In refs 1, 8, and 9, we introduced methods that analyze a portion of the spectrum in both frequency and time domains. These studies have been constructed as a function of temperature and have also been used to evaluate energy redistribution propensities in atmospheric and hydrogen bonded systems. While these studies do facilitate the introduction of composite vibrational mode labels and analyze mode couplings as depicted in refs 1, 2, and 8, these labels depend on the choice of a reference frame or zeroth order modes. In this study, we demonstrate this dependence by choosing multiple zeroth order modes, and in addition we introduce a more general approach derived from the periodic phase space orbits that are sampled during AIMD trajectories. These periodic orbits are constructed using projection operators obtained from a time-translational group that is unique to the dynamics trajectory in question. Our test-bed here is the Zundel cation^{51,52} that has received particular recent attention from both the experimental^{23,24,53–55} and theoretical^{54,56–61} communities. This paper is organized as follows: The methods for spectral analysis are discussed in section 2. Specifically, a new time-translational group analysis technique is introduced in section 2.2 to compute periodic phase space orbits from dynamics data. This facilitates the calculation of modes that include anharmonic effects, as these are sampled during the course of the dynamics trajectories. Techniques to probe and decompose the dynamics data in terms of approximate modes, such as those obtained from the harmonic approximation are also discussed in section 2.1. The latter allows one to gauge the extent to which such “zeroth-order modes” couple during the dynamics process. The approaches discussed in section 2 are applied to the challenging Zundel, H₅O₂⁺ cationic system in the important shared proton stretch frequency region. The results are presented in section 4, and conclusions are given in section 5. A visual illustration of the periodic orbits derived from the method can be found in the Supporting Information.

2. METHODS FOR OBTAINING VIBRATIONAL PROPERTIES FROM DYNAMICS DATA

In *ab initio* molecular dynamics, the molecular framework evolves as a result of forces computed from electronic structure. Hence, it is possible to construct time-correlation functions^{62,63} that account for the dynamical nature of the system. The dynamically averaged vibrational densities of states⁸ are computed from the Fourier transform of the nuclear velocity autocorrelation function (FT-VAC):

$$I_V(\omega) = \lim_{\theta \rightarrow \infty} \int_{t=0}^{t=\theta} dt \exp(-i\omega t) \langle \mathbf{V}(\mathbf{0}) \cdot \mathbf{V}(\mathbf{t}) \rangle$$

$$= \lim_{\theta \rightarrow \infty} \sum_{i=1}^{N_{\text{Atoms}}} \sum_{j=1}^3 \left| \int_{t=0}^{t=\theta} dt \exp(-i\omega t) V_{ij}(t) \right|^2 \quad (1)$$

where the term $\langle \dots \rangle$, in the first equation, represents ensemble average. By contrast, the Fourier transform of the dipole autocorrelation function (FT-DAC) is used to provide peak intensities proportional to the change in dipole moment of the system and, hence, the vibrational spectrum:^{2,3,5,6,62–66}

$$\alpha_{\mu}^{\text{QC}}(\omega) \propto \frac{\omega}{1 - \exp(-\beta\hbar\omega)} \left\{ \omega [1 - \exp(-\beta\hbar\omega)] \lim_{\theta \rightarrow \infty} \int_{t=0}^{t=\theta} dt \exp(-i\omega t) \langle \mu(\mathbf{0}) \cdot \mu(\mathbf{t}) \rangle \right\}$$

$$\propto \omega^2 \lim_{\theta \rightarrow \infty} \sum_{i=1}^3 \left| \int_{t=0}^{t=\theta} dt \exp(-i\omega t) \mu_i(t) \right|^2 \quad (2)$$

The terms inside the curly brackets ($\{ \dots \}$) represent the power normalized absorption cross-section.^{62,63} The prefactor, $\omega/(1 - \exp(-\beta\hbar\omega))$, is a quantum-nuclear correction^{64–66} obtained on the basis of the harmonic approximation. Over a series of publications,^{1–6,8,9,67} it has been demonstrated that these correlation functions provide a good estimate to the vibrational spectrum obtained from experimental action spectroscopy.

We may also write the FT-VAC using mass-weighted velocities: $\tilde{\mathbf{v}}(t) \equiv M^{1/2} \mathbf{V}(\mathbf{t})$, as

$$\tilde{I}_V(\omega) = \int dt e^{-i\omega t} \langle \tilde{\mathbf{v}}(0) \cdot \tilde{\mathbf{v}}(t) \rangle$$

$$= \int dt e^{-i\omega t} \int dt' \tilde{\mathbf{v}}(t') \cdot \tilde{\mathbf{v}}(t' + t)$$

$$= \left| \int dt e^{-i\omega t} \tilde{\mathbf{v}}(t) \right|^2$$

$$= |\tilde{\tilde{\mathbf{v}}}(\omega)|^2 \quad (3)$$

where, the quantity

$$\tilde{\tilde{\mathbf{v}}}(\omega) \equiv \int dt e^{-i\omega t} \tilde{\mathbf{v}}(t) \quad (4)$$

includes information about the characteristic nuclear motions at frequency ω . It is thus possible to derive “modes” that include all information about the dynamically sampled potential surface by analyzing $\tilde{\tilde{\mathbf{v}}}(\omega)$. In sections 2.1 and 2.2, we discuss two frameworks to carry out such an analysis. Specifically, in section 2.1, the $\tilde{\tilde{\mathbf{v}}}(\omega)$ vectors are expressed as linear combinations of a complete set including the Harmonic normal mode vectors obtained from diagonalization of the Hessian matrix and the Jacobi coordinate vectors.^{68–71} The projected components from these linear combinations then yield contributions from the chosen mode vectors onto specific frequencies of the spectrum as depicted within $\tilde{\tilde{\mathbf{v}}}(\omega)$. This leads to a physical interpretation of the spectral feature. By contrast, in section 2.2 we introduce periodic orbits that are constructed from the dynamical evolution of $\tilde{\tilde{\mathbf{v}}}(\omega)$. These periodic orbits are characteristic modes specific to a given frequency window and are obtained from projection operators constructed within a time-translation group.

2.1. Decomposition of $\tilde{I}_V(\omega)$ in eq 3 in Terms of (a) Harmonic Normal Modes and (b) Modes Constructed from Jacobi Coordinates. It is our goal to obtain a physical description of the molecular vibrations responsible for the spectral features seen in the Fourier transformed mass-weighted velocity vectors, i.e., $\tilde{\tilde{\mathbf{v}}}(\omega)$ in eq 4. Toward this, the vectors $\tilde{\tilde{\mathbf{v}}}(\omega)$ are first projected onto the complete, ortho-normal set of

mass-weighted harmonic normal mode coordinates, which are obtained from a static harmonic frequency calculation through diagonalization of the nuclear Hessian matrix constructed on the ground electronic energy surface. As seen in refs 1, 2, and 8, the contribution from each Harmonic normal coordinate at a frequency ω is computed through projection of the frequency dependent mass-weighted velocity in eq 4 onto a given Harmonic normal coordinate as

$$C_i^{\text{Harm}}(\omega) = \vec{H}_i^{\text{Harm}} \cdot \vec{v}(\omega) \quad (5)$$

where \vec{H}_i^{Harm} represents the i th mass weighted harmonic normal mode vector. Since $(1/2)[\vec{v}(\omega) \cdot \vec{v}(\omega)]$ is the kinetic energy at frequency ω , $|C_i^{\text{Harm}}(\omega)|^2$ represents the kinetic energy along mode (or direction) \vec{H}_i^{Harm} at frequency ω . Similarly, the net kinetic energy along the mode vector, \vec{H}_i^{Harm} , inside a frequency window $[\omega_1, \omega_2]$ (under a given peak, for example) may be expressed using the quantity

$$C_i^{\text{Harm}}[\omega_1, \omega_2] = \left(\int d\omega \mathcal{G}_{[\omega_1, \omega_2]}(\omega) |C_i^{\text{Harm}}(\omega)|^2 \right)^{1/2} \quad (6)$$

The quantity $\mathcal{G}_{[\omega_1, \omega_2]}(\omega)$ is a filter function localized inside the frequency window $[\omega_1, \omega_2]$. In this study, the filter function is chosen to be equal to one inside $[\omega_1, \omega_2]$ and zero otherwise. An analysis of eq 6 will provide contributions arising from the mode \vec{H}_i^{Harm} onto the frequency domain $[\omega_1, \omega_2]$. This would lead to a physical interpretation of the spectral feature in question, as described in refs 1 and 8. However, as one might imagine, such a physical interpretation is dependent on the choice of the basis vectors, $\{\vec{H}_i^{\text{Harm}}\}$, and hence in this publication we also carry out a similar analysis using Jacobi coordinates.^{68–71} For consistency, the Jacobi coordinates are mass-weighted and linearized in Cartesian space about the equilibrium geometry just as the harmonic normal coordinates, since they are taken to be locally linear in the small oscillation problem. In this case, eqs 5 and 6 are appropriately modified as

$$C_i^{\text{Jacobi}}(\omega) = \vec{J}_i \cdot \vec{v}(\omega) \quad (7)$$

and

$$C_i^{\text{Jacobi}}[\omega_1, \omega_2] = \left(\int d\omega \mathcal{G}_{[\omega_1, \omega_2]}(\omega) |C_i^{\text{Jacobi}}(\omega)|^2 \right)^{1/2} \quad (8)$$

for the set of mass-weighted Jacobi coordinates $\{\vec{J}_i\}$. The precise transformations between the Jacobi coordinates and the Harmonic coordinates for the Zundel cation are discussed in section 4.1.

2.2. Projected Modes, or Periodic Orbits, Obtained from a Discrete Time Translation Group Constructed from the Dynamics Trajectory. The interpretation of a spectral feature may depend on the choice of basis vectors, $\{\vec{H}_i^{\text{Harm}}\}$ and $\{\vec{J}_i\}$. In this section, we introduce a technique to probe the nature of characteristic molecular motions that contribute to spectral intensity, without reference to a chosen zeroth order basis, and in a manner invariant under coordinate transformation. Toward this, we use the known symmetries present within dynamics trajectories as follows. Since a nonzero spectral intensity at frequency ω implies the presence of a periodic orbit with time-period $\mathcal{T} \equiv \frac{2\pi}{\omega}$ in the trajectory, we may obtain projections of the time evolution of the mass-weighted velocities onto symmetrized phase-space orbits

constructed using the time period \mathcal{T} . Specifically, we construct projection operators $\mathcal{P}_{\mathcal{T}}$, corresponding to frequencies in the spectrum, such that the projection of some function, f , a function of trajectory positions and momenta (or velocities), onto the projected space represented by $\mathcal{P}_{\mathcal{T}}$ is given by

$$\begin{aligned} f_{\mathcal{T}}(t) &\equiv f_{\mathcal{T}}(\mathbf{R}(t), \mathbf{V}(t)) = \mathcal{P}_{\mathcal{T}} f(\mathbf{R}(t), \mathbf{V}(t)) \\ &= \sum_{n=0}^{N_{\mathcal{T},\theta}} f[\mathbf{R}(t + n(\mathcal{T})), \mathbf{V}(t + n(\mathcal{T}))] \end{aligned} \quad (9)$$

where θ is the length of the simulation as seen in eq 1 and $N_{\mathcal{T},\theta}$ is the floor of θ/\mathcal{T} , i.e., the largest integral multiple of \mathcal{T} that remains lower than θ . The corresponding symmetrized mass-weighted velocity vectors are given by

$$\vec{v}_{\mathcal{T}}(t) = \mathcal{P}_{\mathcal{T}}(t) \vec{v}(t) = \sum_{n=0}^{N_{\mathcal{T},\theta}} \vec{v}(t + n(\mathcal{T})) \quad (10)$$

It is clear that $\vec{v}_{\mathcal{T}}(t)$ is the portion of $\vec{v}(t)$ that is periodic with time period \mathcal{T} . Hence, these are periodic velocity orbits. The fact that $\vec{v}_{\mathcal{T}}(t)$ contributes to the spectral intensity may also be noted by further simplifying eq 4 as

$$\begin{aligned} \vec{v}(\omega) &= \int_0^{\theta} dt e^{-i\omega t} \vec{v}(t) \\ &= \left[\int_0^{2\pi/\omega} dt + \int_{2\pi/\omega}^{2(2\pi/\omega)} dt + \dots \right. \\ &\quad \left. + \int_{N_{\mathcal{T},\theta}(2\pi/\omega)}^{\theta} dt \right] e^{-i\omega t} \vec{v}(t) \\ &= \int_0^{2\pi/\omega} dt e^{-i\omega t} \left\{ \sum_{n=0}^{N_{\mathcal{T},\theta}} \vec{v}(t + n2\pi/\omega) \right\} \\ &= \int_0^{\mathcal{T}} dt e^{-i\omega t} \left\{ \sum_{n=0}^{N_{\mathcal{T},\theta}} \vec{v}(t + n(\mathcal{T})) \right\} \\ &= \int_0^{\mathcal{T}} dt e^{-i\omega t} \vec{v}_{\mathcal{T}}(t) \end{aligned} \quad (11)$$

In the above statement, we have assumed that the remainder $[\int_{N_{\mathcal{T},\theta}(2\pi/\omega)}^{\theta} dt]$ signifies a small interval. When that is not the case, the expression above can be suitably modified to include one more cycle within $\vec{v}_{\mathcal{T}}(t)$. In any case, since the intensity at the peak frequency ω may also be obtained from a Fourier transform of $\vec{v}_{\mathcal{T}}(t)$, the corresponding “mode” may be characterized by the time series $\vec{v}_{\mathcal{T}}(t)$. In the results section, we also compute the quantity

$$\vec{v}_{[\omega_1, \omega_2]}(t) \propto \int_{\omega_1}^{\omega_2} d\omega \vec{v}_{\mathcal{T}}(t) \quad (12)$$

which represents the “net-mode” or flux within the frequency window $[\omega_1, \omega_2]$.

2.2.1. The Principal Dynamical Components Determined from $\{\vec{v}_{\mathcal{T}}(t)\}$. It is important to note that the projectors, $\mathcal{P}_{\mathcal{T}}$, and consequently the modes, $\vec{v}_{\mathcal{T}}(t)$, for different values of the period \mathcal{T} may not, in general, be orthogonal. That is, the family of functions $\{\vec{v}_{\mathcal{T}}(t) | \mathcal{T} = \mathcal{T}_{\min}, \dots, \mathcal{T}_{\max}\}$, where

$[\mathcal{T}_{\min}, \mathcal{T}_{\max}] \equiv [2\pi/\omega_1, 2\pi/\omega_2]$ represents some frequency range of interest, may form a nonorthogonal set. In this subsection, we aim to find a characteristic set of orthogonal “modes” constructed from linear combinations of $\{\vec{v}_{\mathcal{T}}(t)\}$ that optimally represent the dynamics in a given spectral range. Toward this, we construct a singular value decomposition (SVD)⁷² of the projected velocities inside a given spectral range. Specifically, the mass-weighted velocity vectors, $\vec{v}_{\mathcal{T}}(t)$, from eq 10 are decomposed as

$$\vec{v}_{\mathcal{T}}(t) \equiv \vec{u}(\omega t, \omega) = \vec{u}(\alpha, \omega) = \sum_i \sigma_i \vec{b}_i(\alpha) \rho_i(\omega) \quad (13)$$

where the first part of the above equation introduces a different function $\vec{u}(\alpha, \omega)$, at each value of ω , that has a periodicity of 2π . The second part of the equality introduces the basis functions $\vec{b}_i(\alpha)$ and $\rho_i(\omega)$ that are essentially obtained from the SVD of $\vec{u}(\alpha, \omega)$. To carry out this SVD represented in eq 13, $\vec{v}_{\mathcal{T}}(t)$ is to be viewed as a matrix, with the following dimensions: (a) one component of the matrix is the product of the number of degrees of freedom and the number of time samples, whereas (b) the other component of the matrix is the number of frequency samples in the range $[\mathcal{T}_{\min}, \mathcal{T}_{\max}] \equiv [\omega_1, \omega_2]$. That is, a three-component entity, $\vec{v}_{\mathcal{T}}(t)$ (the three components being $[t, 3N, \mathcal{T}]$), is interpreted as a two-component matrix to facilitate an SVD within the spectral range $[\omega_1, \omega_2]$. The quantities $\vec{b}_i(\alpha)$ and $\rho_i(\omega)$ are then the associated left and right singular vectors/basis functions pertinent to the chosen spectral range. Specifically, for a given singular value, the quantity, $\rho_i(\omega)$, depends on frequency, and the elements of this function represent the importance of each frequency inside the chosen window in contributing toward $\vec{b}_i(\alpha)$. Similarly, for a given singular value, $b_i(\alpha) \equiv \vec{b}_i(\omega t)$ depends on the number of degrees of freedom and the effective time variable, $\alpha \equiv \omega t$. Hence, $\vec{b}_i(\omega t)$ represents a *collective periodic orbit* that represents the collection of frequency samples in $[\omega_1, \omega_2]$. Such a periodic orbit includes the projections described above and is specific for the spectral range $[\omega_1, \omega_2]$. The prominence of each mode, $\vec{b}_i(\alpha) \equiv \vec{b}_i(\omega t)$, is determined by its associated singular value σ_i , the square of which is proportional to the relative kinetic energy contribution at that particular frequency, just as is the case for the $C_i^{\text{Harm}}(\omega)$ values discussed above following eq 5. Specifically, using the SVD bases, the “net projected mass-weighted velocity” inside the given spectral range is

$$\vec{v}_{[\omega_1, \omega_2]}(t) \propto \int_{\omega_1}^{\omega_2} d\omega \vec{v}_{\mathcal{T}}(t) = \sum_i \sigma_i \int_{\omega_1}^{\omega_2} d\omega \vec{b}_i(\omega t) \rho_i(\omega) \quad (14)$$

and the associated kinetic energy in $[\omega_1, \omega_2]$ is

$$\bar{K}_{[\omega_1, \omega_2]} = \int dt \frac{1}{2} \left| \vec{v}_{[\omega_1, \omega_2]}(t) \right|^2 / \left(\int dt \right) \propto \sum_i \sigma_i^2 \quad (15)$$

where we have used the orthonormality of $\vec{b}_i(\alpha)$ and $\rho_i(\omega)$. In section 4.2, we have used $\{\vec{b}_i(\alpha)\}$ to resolve the spectral properties of the Zundel cation. Specifically, $\{\vec{b}_i(\alpha)\}$ are represented using animations of the $3N$ degrees of freedom in time, and these animations can be found in the Supporting Information.

3. PREVIOUS STUDIES ON THE ZUNDEL CATION

The Zundel cation^{73,74} shown in Figure 1 is a protonated water dimer that has been the focus of several recent experimen-

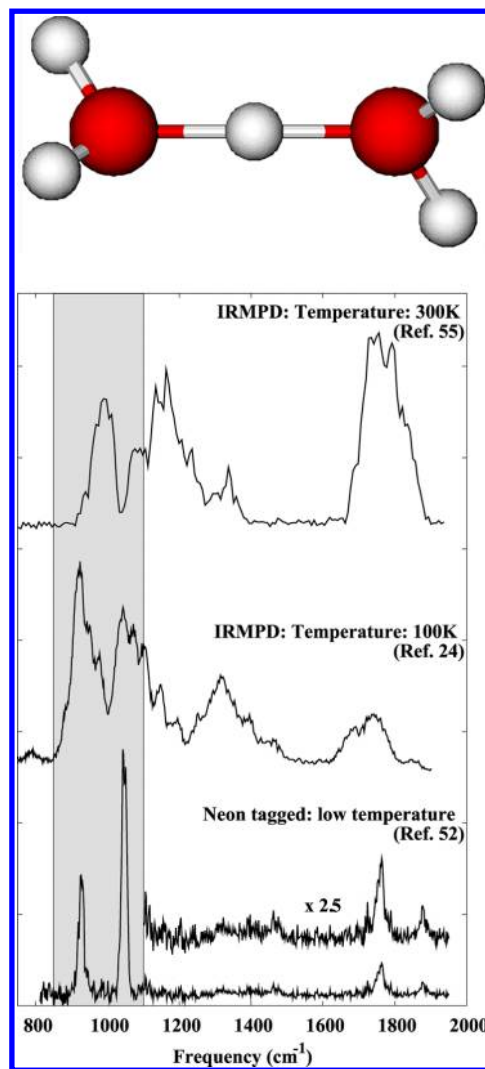


Figure 1. Three experimental action spectra for the Zundel, H_5O_2^+ system: These experimental results are over a range of temperatures and conditions where the top spectrum is from ref 55, the middle spectrum is from ref 24, and the bottom one is from ref 52. This figure is reproduced using the original data in refs 24, 52, and 55. We thank Professors Asmis, Johnson, and Fridgen for providing us with their original experimental data. In each case, the doublet area is highlighted using a gray shade.

tal^{23,24,53–55} and theoretical^{54,56,57,59–61} studies. The methods described in the previous sections are used to probe the spectroscopic behavior of this system. The Zundel cation is a small prototypical system with a proton shared between two water molecules forming a short, strong hydrogen bond.^{75–82} This system plays a fundamental role in the understanding of processes such as the enhanced mobility of protons and deuterons in condensed phase aqueous environments, in biological systems, and in several problems of interest in materials chemistry, such as protonic conductors and fuel cells.

The study of the shared proton spectral features and dynamics in the gas phase Zundel cation began with theoretical work. In ref 56, Vener et al. utilized three separate approaches

to probe the vibrational dynamics in the shared proton spectral region of the Zundel spectrum. (a) By comparing frequencies obtained using the harmonic approximation invoked at optimized nuclear geometries computed at MP2 and Bruckner coupled cluster (B-CCD), the authors found that the proton transfer mode was strongly perturbed by $\sim 300\text{ cm}^{-1}$ at the higher level of theory. (b) To further probe this effect, the authors performed *ab initio* molecular dynamics (AIMD) on an MP2 surface at 360 K, which displayed substantial broadening to highlight a flat surface along the donor–acceptor axis. (c) In a third approach, low lying eigenenergies and transition probabilities for a four-dimensional reduced quantum mechanical Hamiltonian were found. The dimensions chosen were the O–H–O symmetric and antisymmetric stretch (water–water stretch and proton transfer mode) as well as the two perpendicular O–H–O bend modes. The result of this calculation was that bending modes were found at 968 and 1026 cm^{-1} , while the shared proton stretch as well as the second overtone of the O–H–O symmetric stretch coincided at 1158 cm^{-1} giving a rather large intensity. This was interpreted to be a Fermi resonance of the shared proton symmetric and asymmetric stretch modes.

In 2003, a gas-phase experimental spectrum of the shared proton region of the Zundel spectrum was reported by Asmis et al.²⁴ (In Figure 1, we provide all the experimental spectra obtained on this system.) The vibrational spectrum was acquired in that study using infrared multiple photon dissociation (IRMPD).^{18–24} The cluster ions were kept in an ion trap at $\sim 100\text{ K}$ and were conditionally cooled with helium. This was to minimize the hot bands in the spectrum. In the resulting spectrum, three bands at 921, 1043, and 1317 cm^{-1} were found. Consistent with ref 56, the peaks at 921 and 1043 cm^{-1} were assigned to the bending modes, while the shared proton transfer mode was identified with the band at 1317 cm^{-1} . However, a second IRMPD study, by Fridgen et al.,⁵⁵ was blue-shifted in the lower frequency region as compared to the result from ref 24. The cluster temperature was considered to be substantially warmer in ref 55. It was noted that differences in the spectrum and assignments between those from Asmis et al.,²⁴ Fridgen et al.,⁵⁵ and Vener et al.⁵⁶ merited further theoretical and experimental consideration.

Among the studies subsequently undertaken for the Zundel system, investigations spanning the same spectral range using argon and neon tagged vibrational predissociation action spectroscopy were reported by Hammer et al. in ref 52. This experimental work qualitatively represents a second category of spectra in the proton transfer region. Requiring only one photon to dissociate the weakly bound noble gas atom, the spectra were found to have narrower features with significantly less broadening and congestion. The major results were two pairs of peaks around 1000 and 1700 cm^{-1} in the neon and argon tagged spectra with smaller blue-shifted shadow peaks. By varying the number of argons in the cluster, the smaller peaks were attributed to the perturbation introduced by the noble gas messenger atoms. To interpret the spectrum, full dimensional quantum mechanical calculations were performed to obtain eigenstates, energies, and transition energies. The methods utilized were (a) diffusion Monte Carlo,^{83,84} (b) a vibrational self-consistent field study,⁸⁵ MM/VCI,^{86–89} and (c) harmonic frequency calculations obtained at optimized geometries. These approaches were unable to reproduce the doublet at 1000 cm^{-1} and instead found it to be a singlet transition corresponding to the excitation along the proton

transfer mode. Of the two higher frequency peaks, one was attributed to a combination proton transfer + water–water stretch. The findings of this study⁵² were inconclusive as to the nature of the doublet feature at 1000 cm^{-1} . While it was persistent in the experimental spectra, it was unknown as to whether it was intrinsic to the Zundel system or resulting from a perturbation by the messenger atom. Indeed, it was shown in ref 6 that the messenger ion could induce nontrivial perturbations to the overall spectrum, even within the harmonic approximation.

In 2006, Kaledin et al. performed AIMD calculations at 100 and 300 K using a highly accurate fitted potential energy surface.^{57,90} Many trajectories were averaged to compute vibrational spectra. The 100 K spectrum did appear to have a partially resolved doublet around 1000 cm^{-1} . The assignment in this work was done by also computing driven MD simulations⁵⁷ varying the strength of the interacting electric field as well as the frequency of oscillation. At low oscillator strength, the results were in agreement with the harmonic approximation. As the field strength was increased, deviations from their harmonic spectrum were noted. The time average of the position vector projected onto the harmonic normal coordinates provided information about the modes that contribute at each frequency. On the basis of these data, it was concluded that the 1000 cm^{-1} doublet was due to the shared proton stretch coupled to torsion, with the lower frequency having more of the proton stretch character. Subsequently, Vendrell et al.^{59–61} employed full-dimensional multiconfiguration time dependent Hartree method (MCTDH)^{33,47,91} using the same accurate potential used in ref 54. This resulted in an IR vibrational spectrum in excellent agreement with the experimental neon tagged vibrational predissociation spectrum.⁵² Analysis was performed by computing approximate eigenstates corresponding to each doublet peak and projecting them onto zeroth order states defined by Jacobi coordinates. Two zeroth order modes were found to be dominant in describing the doublet. The first mode represented an excitation along the shared proton coordinate parallel to the O–O axis. The second was a combination constructed by one excitation in the water–water stretch together with the asymmetric double excitation of the water wag (pyramidalization) coordinates. The interpretation was that the observed doublet at 1000 cm^{-1} could be identified as a Fermi resonance between the two above-defined zeroth order states, with the higher frequency band containing mostly proton transfer and the lower peak acquiring more water–water stretch/asymmetric wag. The two results published by Kaledin et al.⁵⁷ and Vendrell et al.,^{59–61} using the same potential energy surface, together with the tagged predissociation spectra of Hammer et al.,⁵² seem finally to be converging in the direction of a unified story.

There are still uncertainties and inconsistencies however. The higher temperature IRMPD results remain unresolved with no study to date providing a uniform picture over the entire temperature range. Here, we model the spectrum over the entire temperature range using a single computational method. To analyze the spectral features thus obtained, we utilize the tools discussed in sections 2.1 and 2.2.

With regards to the blue shift at low frequencies noted by comparison of the IRMPD spectra in refs 24 and 55, it is useful to state a related result found in refs 1 and 2, concerning the deuteron and proton bound dimethyl ether dimer. As noted in Figure 2, simulations similar to those constructed in this

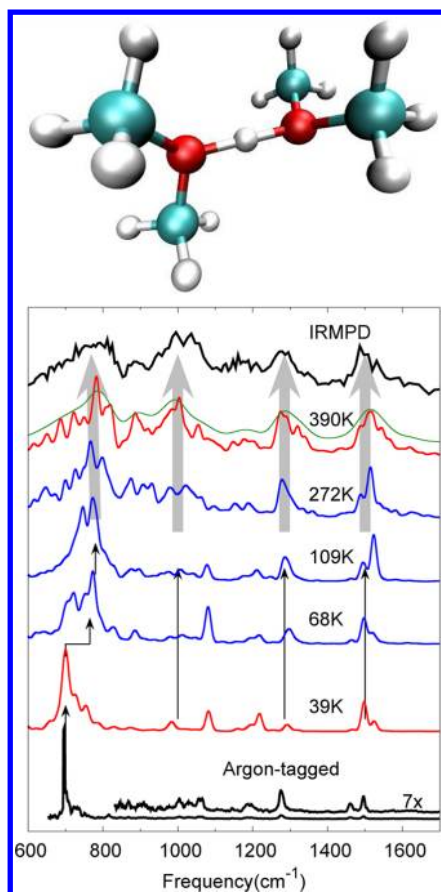


Figure 2. The progression of finite temperature AIMD spectra for $[\text{Me}_2\text{O}-\text{D}-\text{OMe}_2]^+$, as discussed in ref 1: This system can be viewed as a generalization of the Zundel cation, $[\text{H}_2\text{O}-\text{D}-\text{OH}_2]^+$. The $\alpha_\mu^{\text{QC}}(\omega)$ intensities (see eq 2) computed from 39 K AIMD trajectories, at the B3LYP/6-31+G** level of theory (shown in red), reproduce the argon-tagged spectrum²⁵ well, whereas the 390 K result (red) reproduces the IRMPD spectrum.¹ The AIMD spectra at intermediate temperatures (blue) “interpolate” between the two experimental results. Notably the primary, shared hydrogen transfer peak at 39 K shifts at 68 K and then dominates at higher temperatures. This blue-shift is quite similar to that found for the higher temperature spectra here, see Figures 1 and 3. All spectra here are filtered in the frequency domain using a Gaussian with full-width half-max $\approx 15.3 \text{ cm}^{-1}$. On account of a rotational broadening, a spectrum filtered using a full-width half-max of about 50 cm^{-1} (green trace) is also provided.

publication recover the differences between the argon-tagged action and IRMPD spectroscopic results. A similar blue-shift as that observed in Figure 1 is also noted in Figure 2, which depicts the behavior for $[\text{Me}_2\text{O}-\text{D}-\text{OMe}_2]^+$, a “chemical generalization” to the Zundel system. This aspect has been probed deeply in ref 1. It appears that the sometimes nontrivial differences in the results from these experiments can be explained through ab initio dynamics simulations on a single electronic surface with temperature as the single differentiating parameter.

4. SIMULATING THE VIBRATIONAL DENSITY OF STATES AND THE DIPOLE SPECTRA FROM DYNAMICS SIMULATIONS

In this section, we investigate the vibrational dynamics and spectroscopy under gas phase and constant energy (micro-canonical NVE ensemble) conditions. The latter is critical because time-correlation functions are to be computed to obtain the density of states. These necessitate a conserved Hamiltonian during dynamics. The gas-phase calculations correctly mimic the experimental conditions. The simulations followed classical mechanics of the nuclei on a potential energy due to the electronic degrees of freedom separated according to the Born–Oppenheimer approximation. The calculations were carried out using a development version of the Gaussian suite of quantum chemistry programs.⁹² The potential energy used in these calculations is a fitted CCSD(T) constructed by Bowman et al.⁹⁰ In the case of the fitted potential, numerical gradients were implemented in the Gaussian development version⁹² to compute the forces for the classical nuclear dynamics. This calculation involved a 17-point derivative along each atomic coordinate, derived by Taylor expansion of the values of the potential on an evenly spaced grid centered on the point of interest, the point about which the terms of the Taylor series is evaluated. In addition, any rotational or translational components arising due to limitations in computational precision were projected out at every step. The resulting dynamics maintained energy conservation quite well, as seen in the Table 1. Trajectories were constructed for a range of temperatures. The chosen temperature range, also shown in Table 1, includes the regime of operation of the argon-tagged as well as IRMPD experiments as noted in refs 1, 2, 5, and 6.

The dipole spectra are computed using eq 2 and shown in Figures 3a, 3b, 3c, and 3d. Specifically, Figure 3a depicts the entire calculated spectral range, while Figure 3b shows the range over which experimental results are generally available. The critical doublet region is the focus of Figure 3c. The following features are evident from these figures: (a) Figure 3b shows three regions of spectral intensity. The doublet at 1000 cm^{-1} , which is seen in the low temperature experimental spectrum,⁵² is resolved in the simulated spectra between 26 and 67 K, as also noted in Figure 4. (b) The 1800 cm^{-1} peak is found in all spectra, and the feature at 1500 cm^{-1} loses resolution with increased temperature. (c) In the high temperature experimental spectra,^{24,55} the broadened 1000 cm^{-1} doublet was blue-shifted with an increase in temperature. This aspect can be seen in our computations in Figures 3b and 3d. While this peak shifting is generally recovered in the simulated spectra here, particular contours of the peaks from experimental results were not recovered at high temperatures in the dipole spectra.

The doublet around 1000 cm^{-1} was previously described to be the signature of the shared proton stretch vibrational mode. As such, this feature is the central focus of this study. The simulated trajectories at energies with corresponding temperatures of 26 K through 67 K reproduce the doublet at 870 and 990 cm^{-1} , as seen in Figure 3b. (All spectra provided in this

Table 1. Temperature and Energy Conservation Properties for the Various AIMD Trajectories. Total Simulation Time in Each Case is 20 ps, with a Time-step of 0.25 fs

temp (K)	13 ± 4	16 ± 4	26 ± 6	33 ± 8	40 ± 10	67 ± 17	123 ± 29	237 ± 56	475 ± 109
$\Delta E (10^{-4} \text{ kcal/mol})$	1.5	2.1	4.2	6.3	8.6	16.6	27.4	42.6	89.7

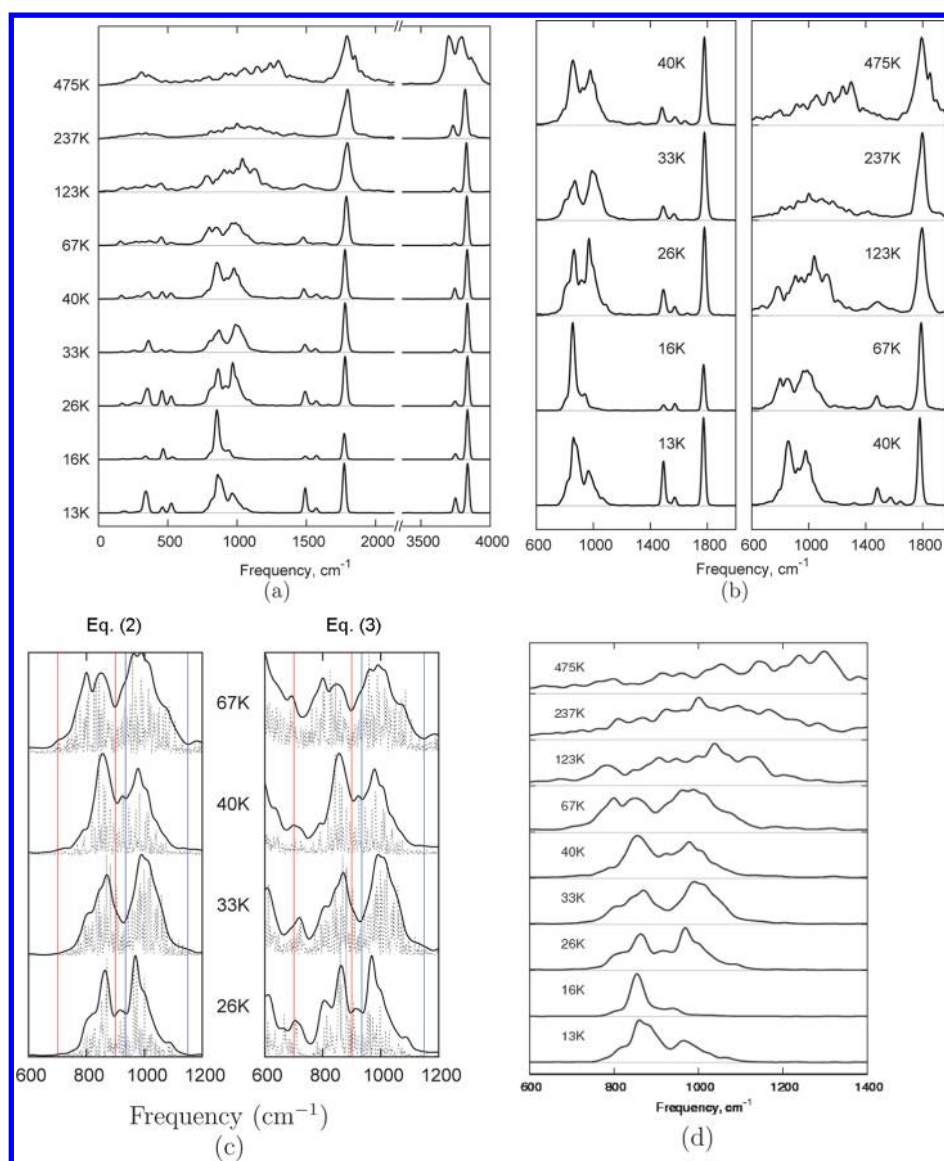


Figure 3. (a) The dipole spectrum as given by eq 2. Each spectrum is independently normalized. (b) The same over a typical frequency range noted in IRMPD and argon-tagged action spectroscopy experiments. (c) The dipole spectrum, as per eq 2 on the left, and the velocity spectrum, as per eq 3 on the right. Part c focuses on the doublet region. The broadening and blue-shift of the 1000 cm^{-1} spectral region, as a function of temperature, is the subject of part d. A Gaussian convolution of 11 cm^{-1} standard deviation was added to these spectra and shown with solid lines; the raw data are also shown using dashes in part c. This Gaussian filter is applied to all spectra in this study and is consistent with that used in ref 2.

studied have been convoluted with a Gaussian filter of width 11 cm^{-1} in the frequency domain. This filter is consistent with the rotational broadening seen in some of these experimental studies.¹⁾ Higher temperature trajectories exhibit significant spectral broadening (see Figure 3a and b); however, all features seen in the experimental spectra (shown in Figure 1) are approximately reproduced. The choice of temperatures in this study is based on previous work^{1,5,6} where it has been shown that low temperature AIMD results are in agreement with argon-tagged single photon experiments, and higher temperature results are in agreement with those from IRMPD.

4.1. Results from Vibrational Decomposition of Finite Temperature Spectra in Terms of (a) Harmonic Normal Modes and (b) Modes Constructed from Jacobi Coordinates. In order to obtain a physical description of the characteristic vibrations in the system that give rise to the individual peaks of the doublet, the Fourier transformed mass-

weighted velocity vectors were projected onto (a) the harmonic normal mode coordinates, obtained by a static harmonic frequency calculation at the density functional level of theory, and (b) mass-weighted Jacobi coordinates, as described in section 2.1. Equations 16–19, below, define the mass-weighted, symmetrized, Jacobi coordinates in terms of the harmonic coordinates. Similarly, eqs 20–23 represent the inverse transformation of the harmonic coordinates in terms of the mass-weighted, symmetrized, Jacobi coordinates.

$$\begin{aligned} \gamma_{\text{Asym}} = & -0.97 \cdot (w - w_{\text{A-Wa}}^{306}) + 0.17 \cdot (H_{\parallel} w_{\text{A-Sc}}^{1001}) \\ & - 0.12 \cdot (w_{\text{A-Sc}} H_{\parallel}^{1761}) \end{aligned} \quad (16)$$

$$\begin{aligned} \gamma_{\text{Sym}} = & -0.98 \cdot (w - w_{\text{S-Wa}}^{375}) - 0.12 \cdot (w - w_{\text{Tw}}^{197}) \\ & - 0.11 \cdot (w_{\text{S-Sc}} H_{\perp}^{1678}) \end{aligned} \quad (17)$$

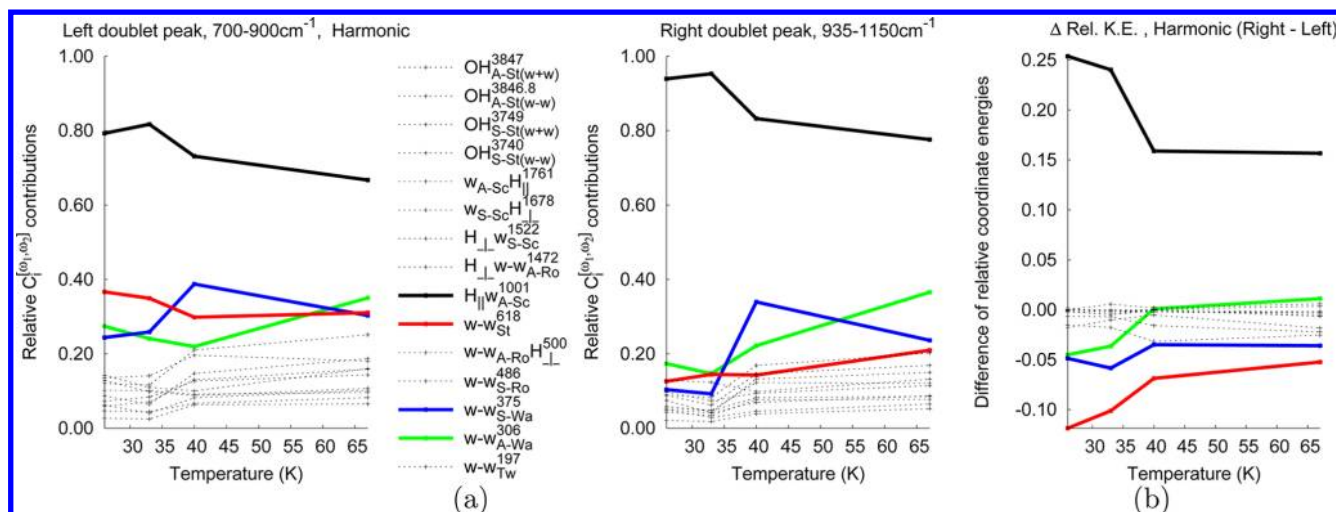


Figure 4. (a) The contributions from the individual mass-weighted harmonic mode coordinates toward the peaks of the doublet. The quantity shown in part a is the $C_i^{\text{Harm}}[\omega_1, \omega_2]$ coefficient from eq 6, where the values for ω_1 and ω_2 are listed in the figure. The proton transfer, water–water stretch, and water wagging modes are depicted using solid lines and described following eq 19. Since $|C_i^{\text{Harm}}[\omega_1, \omega_2]|^2$ represents the kinetic energy within the frequency window $[\omega_1, \omega_2]$ in the harmonic mode i , part b displays the difference in kinetic energy within a given mode, between the two frequency windows. A positive value signifies more energy in the right peak and a negative value denotes more energy in the left peak.

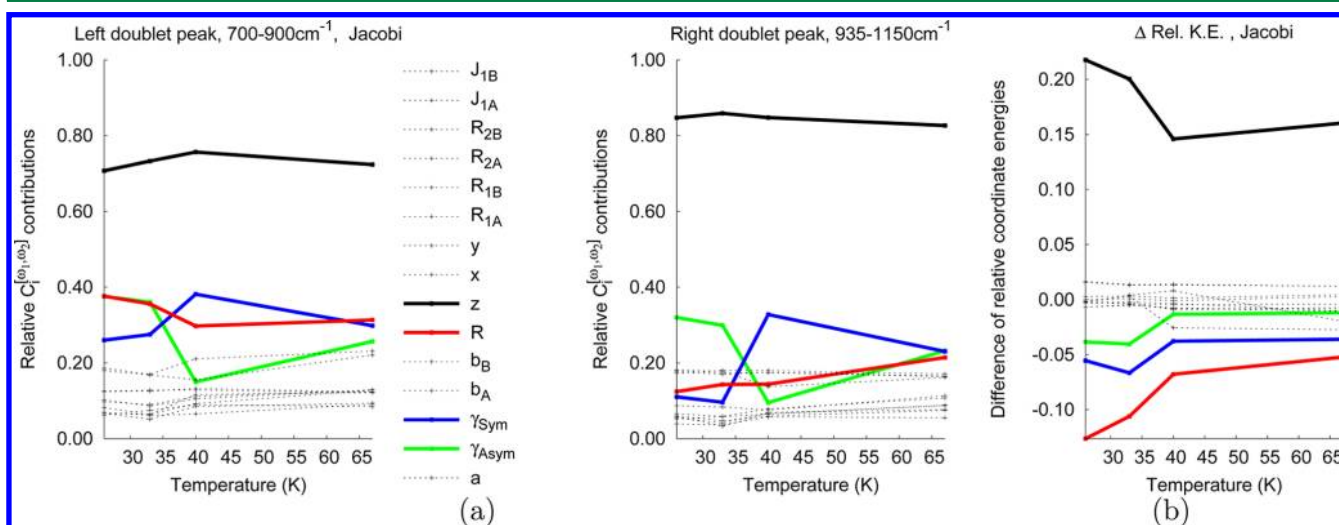


Figure 5. (a) The contributions from the mass-weighted Jacobi coordinates toward the individual peaks of the doublet. The quantity shown in part a is the $C_i^{\text{Jacobi}}[\omega_1, \omega_2]$ coefficient from eq 8, where the values for ω_1 and ω_2 are listed in the figure. As in Figure 4a, the proton transfer mode, water–water stretch, and water wagging modes are depicted using solid lines and described following eq 19. The water wags are symmetric and asymmetric combinations of the original single water wag coordinates. See eqs 16 and 17 for g_{Sym} and g_{Asym} . Since $|C_i^{\text{Jacobi}}[\omega_1, \omega_2]|^2$ represents the kinetic energy within the frequency window $[\omega_1, \omega_2]$ in the harmonic mode i , part b displays the difference in kinetic energy in a given mode, between the two frequency windows. A positive value signifies more energy in the right peak, and a negative value denotes more energy in the left peak.

$$R = -0.99 \cdot (w - w_{\text{St}}^{618}) - 0.16 \cdot (w - w_{\text{S-Ro}}^{486}) \quad (18)$$

$$z = -0.89 \cdot (H_{\parallel} w_{\text{A-Sc}}^{1001}) + 0.39 \cdot (w_{\text{A-Sc}} H_{\parallel}^{1761}) - 0.20 \cdot (w - w_{\text{A-Wa}}^{306}) + 0.11 \cdot (H_{\perp} w - w_{\text{A-Ro}}^{1472}) \quad (19)$$

Here, γ_{Sym} , γ_{Asym} , R , and z are the symmetric and asymmetric water wags, the oxygen–oxygen stretch, and the shared proton motion along the oxygen–oxygen axis, respectively, in the Jacobi coordinate system. The corresponding eigenvectors of the Hessian that contribute significantly to the Jacobi coordinate transformation are $(w - w_{\text{A-Wa}}^{306})$ and $(w - w_{\text{S-Wa}}^{375})$, which represent the antisymmetric and symmetric water wag, $(H_{\parallel} w_{\text{A-Sc}}^{1001})$ and $(w_{\text{A-Sc}} H_{\parallel}^{1761})$ are antisymmetric and symmetric linear combinations of axial proton motion coupled to the

scissor motion of the water molecules, and $(w - w_{\text{St}}^{618})$ is the water–water stretch. As noted from eq 19, the proton transfer coordinate is the least “pure” of the four, involving the asymmetric water scissor ($w_{\text{A-Sc}} H_{\parallel}^{1761}$) and asymmetric water wag ($w - w_{\text{A-Wa}}^{306}$). This is what we would expect from the harmonic proton transfer coordinate since it represents a water/hydronium pair interconversion. Similarly, as seen below in eq 20, the harmonic asymmetric water wag includes proton transfer motion. Furthermore, to maintain consistency between the two coordinates, the two Jacobi single-water wags were combined using the symmetric and asymmetric harmonic water wag coordinates.

$$w - w_{\text{A-Wa}}^{306} = -0.97 \cdot (\gamma_{\text{Asym}}) - 0.20 \cdot (z) \quad (20)$$

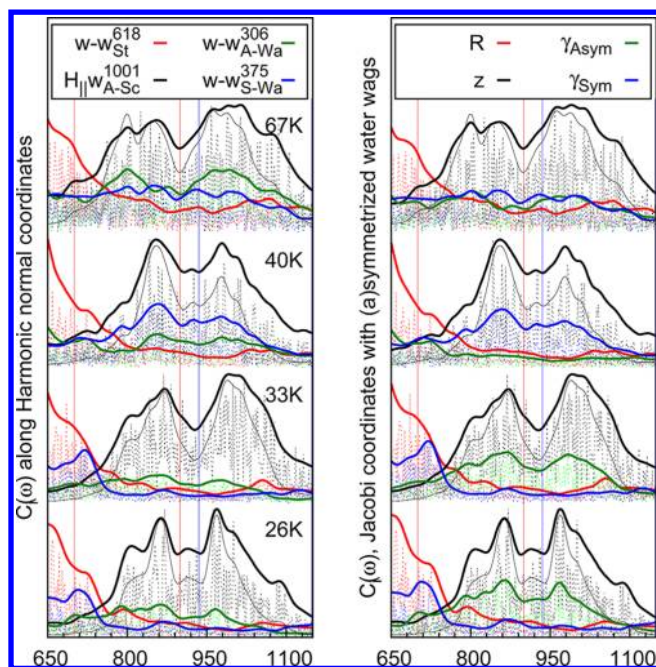


Figure 6. Harmonic (left) and Jacobi (right) coordinate contributions to the velocity spectra at various temperatures. These contributions are calculated as given in eqs 5 and 7 (units of $(K.E.)^{1/2}$). The four previously identified important coordinates are plotted (proton transfer, black; water–water stretch, red; asymmetric water wag, green; symmetric water wag, blue) along with the dipole spectrum (thin black line). [Also see Figures 4 and 5 for reference.]

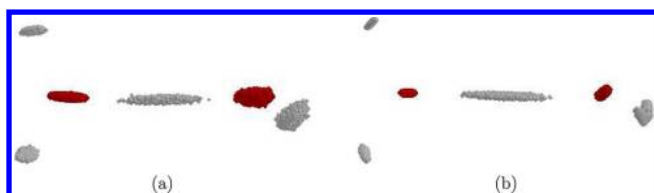


Figure 7. Net projected velocity as given by eq 12 for the 700–900 cm^{-1} (a) and 935–1150 cm^{-1} (b) frequency components of the doublet band at 26 K. Note: the two waters in each image are related by reflection and a 90° rotation about the water–water torsion angle.

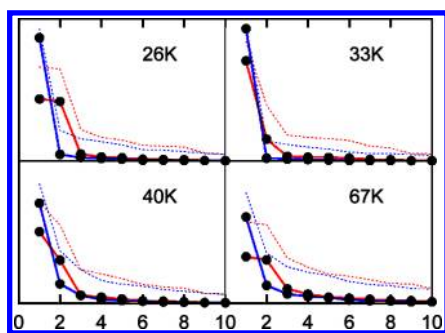


Figure 8. Singular values, σ_i , from eq 14, and the squared singular values, σ_i^2 , for the first 10 SVD basis functions. The lower frequency region of the doublet, 700–900 cm^{-1} , is shown in red, while the higher frequency region, 935–1150 cm^{-1} , is shown in blue. The dotted lines correspond to the singular values, σ_i , and the solid lines are the squared counterparts.

$$w-w_{S-Wa}^{375} = -0.98 \cdot (\gamma_{Sym}) \quad (21)$$

$$w-w_{St}^{618} = -0.99 \cdot (R) \quad (22)$$

$$H_{||}w_{A-Sc}^{1001} = -0.89 \cdot (z) - 0.23 \cdot (R_{1A}) + 0.23 \cdot (R_{1B}) - 0.18 \cdot (R_{2A}) + 0.18 \cdot (R_{2B}) + 0.17 \cdot (\gamma_{Asym}) \quad (23)$$

In this section, the dynamically averaged vibrational densities of state represented by eq 1 are decomposed in terms of both the eigenvectors of the Hessian as well as the Jacobi coordinates to gauge the spectral behavior, in the doublet region, as a function of the temperature.

In Figure 4a, the relative contributions along harmonic normal coordinates are plotted at various temperatures for the two bands defined over the frequency ranges 700–900 cm^{-1} and 935–1150 cm^{-1} . The major contributors are the proton transfer motion (black, solid), water–water stretch (red, solid), and symmetric and asymmetric water wag modes (blue and green solid, respectively). These coordinates also describe the most prominent differences between the two peaks, as can be seen in Figure 4b, where the differences between the relative energies in each mode are plotted. Figure 4b shows that the largest difference between the two peaks of the doublet is due to the reduced importance of the proton transfer mode (black) replaced by increased importance of the water–water stretch (red) followed by the water wags, symmetric then asymmetric (blue and green).

This is qualitatively reminiscent of the zeroth order interpretation of the fully quantum mechanical results reported by Vendrell et al.^{59–61} Vendrell et al. noted an increased prominence of a zeroth order combination mode involving Jacobi water–water stretch and an asymmetric eigenfunction of the two Jacobi (single) water wag coordinates. Upon comparison, we see in Figure 4b that the same basic set of modes differentiates the two peaks of the doublet here as well. However, the mode descriptor that contributes in the study by Vendrell et al. is a two-variable correlated combination of the water–water wag and the water–water stretch. In our case, while these same modes do contribute, the zeroth order basis of molecular motions does not include a correlated combination (although the dynamics trajectories do include such a correlated combination). Furthermore, the temperature dependences of these differences are nontrivial. Upon comparison with Figure 3d, we note that (a) the doublet gets “washed out” as the temperature is increased and (b) the difference in contribution from the asymmetric wag reduces with increasing temperature. But Figure 4b displays a narrower temperature range as compared to Figures 3b and 3d.

The results using the Jacobi coordinate system (Figure 5a and b) are qualitatively equivalent to those from the harmonic coordinates. The highest contributors include the proton excursion along the water–water axis (black), water–water center of mass distance oscillation (red), and the symmetric and asymmetric combinations of the single-water wags (blue and green). However, it is also clear upon inspection of Figures 4b and 5b that the qualitative description of differences between the two peaks varies depending on the choice of zeroth order modes (or choice of reference frame used to decompose the molecular motion). Notwithstanding the subtle differences between the decompositions in terms of harmonic and Jacobi frames, the final picture remains qualitatively similar, in particular, the increased prominence of the water–water stretch and water wag modes in the lower frequency

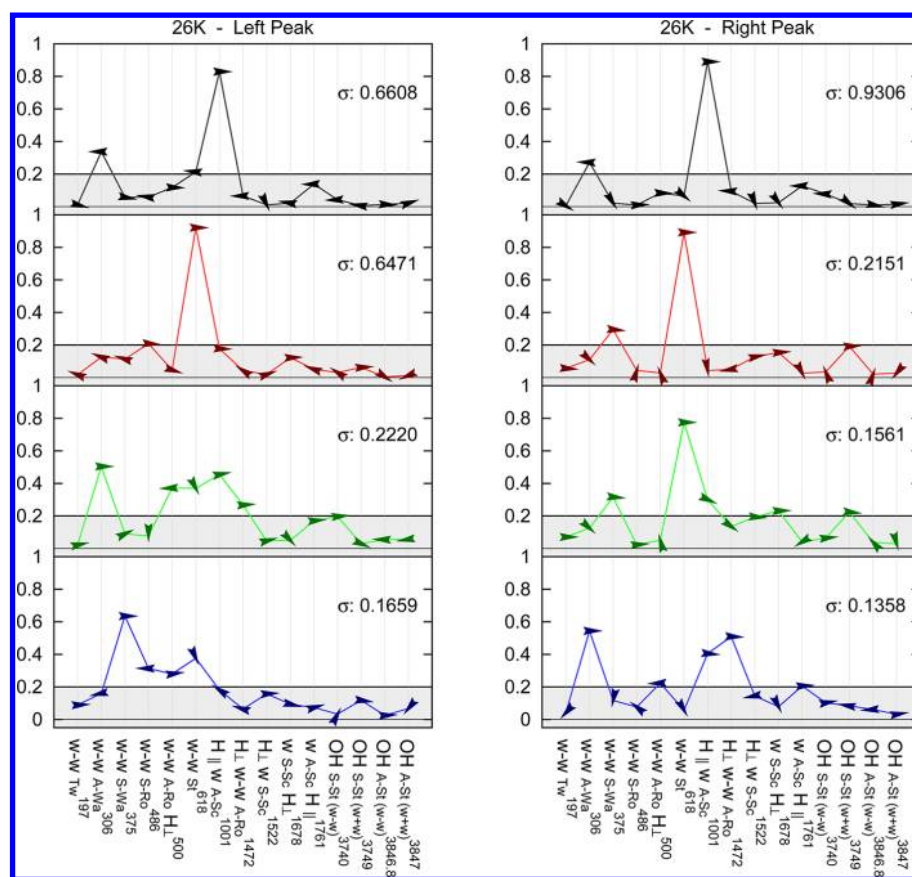


Figure 9. Harmonic normal mode components of SVD basis functions, $C_i^{\text{Harm}}[\vec{b}_i]$ in eq 24, for the 26 K doublet peaks. Arrows indicate the relative phase along coordinates associated with the fundamental harmonic in the Fourier series of \vec{b}_i . See eq 25.

component of the doublet peak seen in Figure 5b. In addition, the symmetric water wag differentiates the left peak more than the asymmetric wag.

In the above analysis, as per eqs 6 and 8, the $C_i^{\text{Harm}}(\omega)$ and $C_i^{\text{Jacobi}}(\omega)$ coefficients were integrated in the frequency range $[\omega_1, \omega_2]$ to obtain the cumulative contributions shown. However, it is also possible to simply inspect the integrand in eqs 6 and 8 as a function of frequency and temperature. Such an analysis is carried out in Figure 6, where the spectral distributions are plotted without integrating for the four critical harmonic and four Jacobi coordinates. In addition, Figure 6 also includes the spectrum in Figure 4 that is superimposed using thin black lines. One of the most striking features from Figure 6 is that the dipole spectrum is basically reproduced by simply following the proton stretch mode, $(H_{\parallel}W_{A-Sc}^{1001})$, as a function of frequency. This striking feature is also reminiscent of the study in ref 1 where again the spectral features and associated temperature dependence of a proton-bound ether dimer, “a chemical generalization of the Zundel system” treated here, were qualitatively reproduced by simply following a single shared proton stretch mode, compare with Figures 7 and 8 in ref 1 along with the accompanying discussion. In retrospect, this here, as in ref 1, is not a surprise since the shared proton stretch has the largest dipole transition intensity. Another interesting aspect is the tail of the water–water stretch overlapping the lower frequency peak from the doublet. The fact that this peak shows up in the integrated intensities in Figures 4a and 5a is due to the choice of $\mathcal{G}_{[\omega_1, \omega_2]}(\omega) = 1$ in eqs 6 and 8. Future studies will include a smoother filtering, but it is already clear that the dipole spectrum in this system is also dominated by the

shared proton stretch. Another feature readily apparent is that, over the span of the doublet, the relative prominence of the symmetric and asymmetric water wag coordinates is not consistent across temperatures. For the 26 and 33 K spectra, the asymmetric wag seems to contribute across the doublet more. As the temperature of the trajectory is increased to 40 K, this ordering switches such that the symmetric wag coordinate dominates over the asymmetric. This suggests that the proton transfer coordinate couples to both wag coordinates with the relative intensity of interaction being dependent on the total energy, and thus the potential surface sampled.

4.2. Results from Inspection of the Periodic Phase Space Orbits. We now inspect the actual molecular motions sampled during dynamics using the time-translation group analysis presented in section 2.2. Reconstructing the motion responsible for the spectral features in a given frequency range is accomplished through eq 12. In Figure 7, we represent the quantity $\vec{v}_{[\omega_1, \omega_2]}(t)$ in eq 12 by superimposing the entire set of time samples into a single figure. Thus, atoms that sample a larger portion of the configurational space during dynamics appear thicker in Figure 7, and vice versa. As can be seen, the space sampled in the lower frequency band is more spread out as compared to the higher frequency peak. For the case of the latter, the proton follows a transfer path alongside concurrent water scissor and wag modes. The proton behaves similarly in the lower frequency peak, but the water molecules sample oblong-shaped disk-like regions within their respective projected three-dimensional spaces. These are stretched primarily in the direction of the O–O axis, indicating more diversity in motion under the lower frequency peak, especially

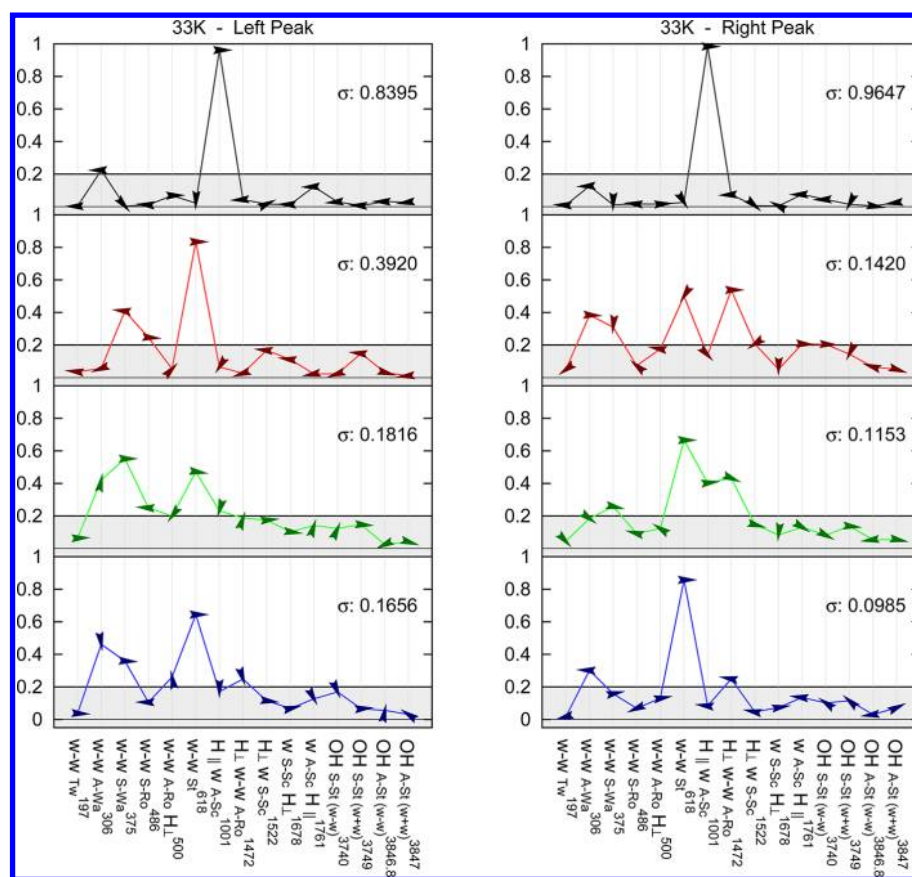


Figure 10. Harmonic normal mode components of SVD basis functions, $C_i^{\text{Harm}}[\vec{b}_j]$ in eq 24, for the 33 K doublet peaks. Arrows indicate the relative phase along coordinates associated with the fundamental harmonic in the Fourier series of \vec{b}_j . See eq 25.

coupled to the OO stretch. This aspect is qualitatively similar to the result seen in both the harmonic as well as Jacobi coordinate decompositions, where again, the OO stretch was seen to contribute to a greater extent at the lower end of the doublet region.

A set of characteristic modes of vibration are determined through singular value decomposition (SVD) of the set of all projected velocities as discussed in section 2.2.1. Figure 8 displays the singular values, and it can be seen that only the first few basis functions represent the majority of the kinetic energy (see eqs 14 and 15). Graphical representations of the first four basis functions at each temperature are presented in the Supporting Information. These provide a representation of the molecular motions captured within each basis. To be clear, the animations here include the full anharmonicity of the potential as sampled at a given temperature and are, in fact, the orthonormal periodic orbits sampled during dynamics.

To quantitatively analyze the time-dependent picture introduced through the $\{\vec{b}_i(\alpha)\}$ basis vectors, we choose to represent these in terms of the $C_i^{\text{Harm}}(\omega)$ vectors. We note that while the time evolution of the mode, $\{\vec{b}_i(\alpha)\}$, is explicitly noted, those for $C_i^{\text{Harm}}(\omega)$ and $C_i^{\text{Jacobi}}(\omega)$ follow analytically since these are solutions to the harmonic problem. Furthermore, the square root of the relative kinetic energy along harmonic normal mode coordinates for a given SVD basis function is computed as

$$C_i^{\text{Harm}}[\vec{b}_j] = \left(\int d\alpha \hat{H}_i^{\text{harm}} \cdot \vec{b}_j(\alpha)^2 \right)^{1/2} \quad (24)$$

The quantity $\hat{H}_i^{\text{harm}} \cdot \vec{b}_j(\alpha)$ is a dot-product in $3N$ space, that is the number of nuclear degrees of freedom, and the integration is over the reduced time variable α . This quantity parallels that given in eq 6. The quantity from eq 24 is presented in Figures 9–12 to provide an interpretation of the $\{\vec{b}_i(\alpha)\}$ basis vectors in terms of the commonly used harmonic modes. In addition, since $\vec{b}_i(\alpha)$ is a periodic function, it can be expanded using a Fourier series as

$$\vec{b}_j(\alpha) = \sum_{j=1}^{3N} b_{j1} \sin(\alpha - \phi_{j1}) \hat{H}_i^{\text{harm}} + \sum_{j=1, k=2}^{3N, \infty} b_{ijk} \sin(k\alpha - \phi_{ijk}) \hat{H}_i^{\text{harm}} \quad (25)$$

The phases, $\{\phi_{ijk}\}$, then represent the phase shifts required in $\vec{b}_i(\alpha)$ to match the sinusoidal component. In Figures 9–12, we also include arrows representing the relative phase of motion along each separate harmonic coordinate. Here, these quantities are defined as the phase, ϕ_{j1} , of the fundamental harmonic in the Fourier expansion of the SVD basis function depicted in eq 25.

In the section below, the quantities ϕ_{j1} and $C_i^{\text{Harm}}[\vec{b}_j]$ are analyzed to interpret the $\{\vec{b}_i(\alpha)\}$ basis vectors and gauge the invariance of the spectral interpretation with coordinate transformation since the quantities in eqs 24 and 25 depict the projections of $\vec{b}_i(\alpha)$ onto $\{\hat{H}_i^{\text{harm}}\}$.

4.2.1. Description of SVD Basis Functions: $\vec{b}_j(\alpha)$. The most significant SVD basis functions, for the temperature range considered in Figures 9–12, are directed primarily along the proton transfer and water–water stretch harmonic normal

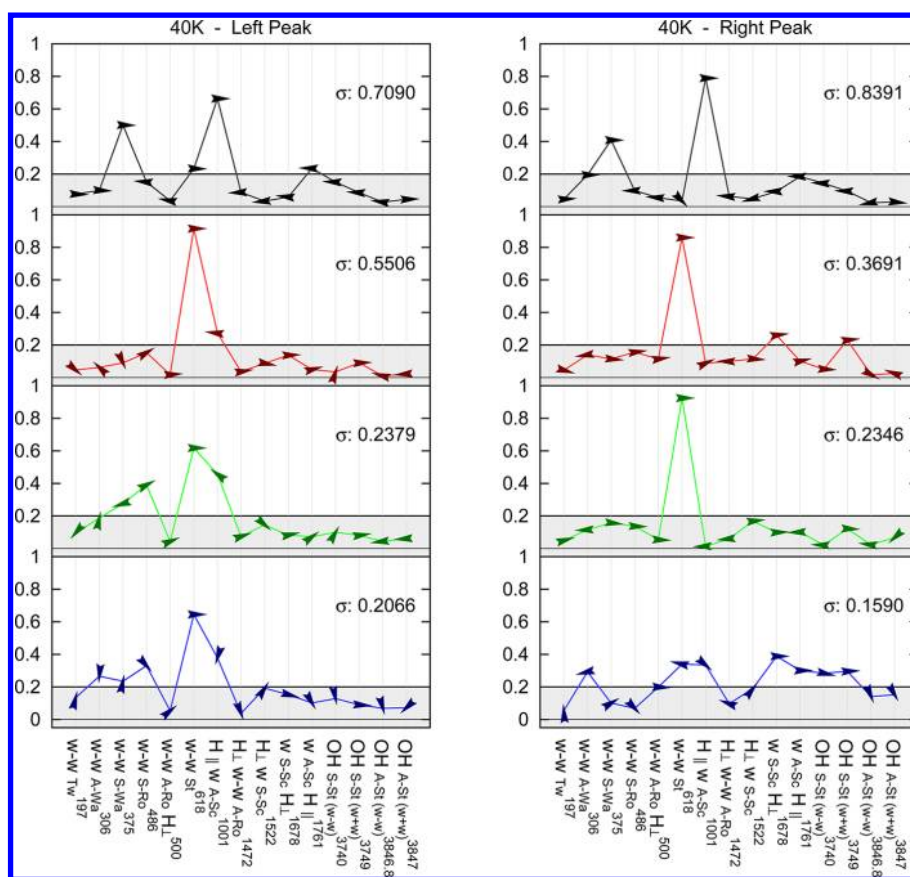


Figure 11. Harmonic normal mode components of SVD basis functions, $C_i^{\text{Harm}}[\vec{b}_i]$ in eq 24, for the 40 K doublet peaks. Arrows indicate the relative phase along coordinates associated with the fundamental harmonic in the Fourier series of \vec{b}_i . See eq 25.

coordinates. In nearly all the cases, the first basis function corresponds to the proton transfer motion, while the second is along the water–water stretch coordinate. An important exception is the 67 K data provided in Figure 12. The first two basis functions representing the motion of the left doublet peak are not divided into proton transfer and water–water stretch but are rather into out-of-phase and in-phase motions along the two coordinates, representative of a general trend in which increased mixing follows an increased dynamics temperature. This example is also an exception in that the motion for the first, as well as the second, basis function is not led by the proton transfer but rather the motion along the water–water stretch.

Comparing across the two peaks, the right doublet peaks are dominated by motion directed largely along the proton transfer axis, while the left doublet peaks contain an increased contribution of motion along the water–water stretch, evidenced by the trends of the first and second singular values in graphical representations provided in the Supporting Information. This observation is in agreement with the coordinate based analyses given above, seen in Figures 4b and 5b where it is shown for all temperatures that the right peak contains proportionally more kinetic energy along the proton stretch axis and the left along the water–water stretch.

The symmetric and asymmetric water wag modes participate in the SVD basis functions in two ways. First, the water wags often contribute to the third and fourth basis functions, with various couplings to the proton transfer, water–water wag, and water rocking coordinates. In the first two basis functions, which contribute much more to the total energy, motion along

the water wag coordinates provides a minor part of the coordinate description to the more prominent proton stretch and water–water stretch motions. This particular aspect is consistent with that seen in Figure 6, where we note that the wag contributions are small as a function of frequency but significant as indicated in the corresponding integrated plots, Figures 4a and 5a.

5. CONCLUSION

A number of detailed studies have been performed with respect to the $\sim 1000 \text{ cm}^{-1}$ doublet spectral feature of the Zundel protonated water dimer, both experimentally and computationally,^{24,52,55–57,59–61,93} of which selected studies have been analyzed. Depending on the particular theoretical and experimental treatments, investigations have arrived at somewhat disparate explanations of the mechanism causing the peak splitting. In all cases, it was interpreted as a coupling of vibrational modes in which the zeroth order picture failed to reproduce the doublet. Among the zeroth order modes implicated in the spectral features around 1000 cm^{-1} were the proton transfer motion, perpendicular proton motions, water–water stretch, water wagging modes, and water–water torsion, as referenced in the Introduction.

In this study, two methods were introduced to analyze *ab initio* molecular dynamics trajectories that were obtained here. In the first case, an averaged overlap of the velocity Fourier transform onto harmonic (and Jacobi) coordinates was computed over the frequency ranges of the two doublet peaks, see eqs 6 and 8 and section 2.1. The analysis implicates the proton transfer and the water–water stretch as differ-

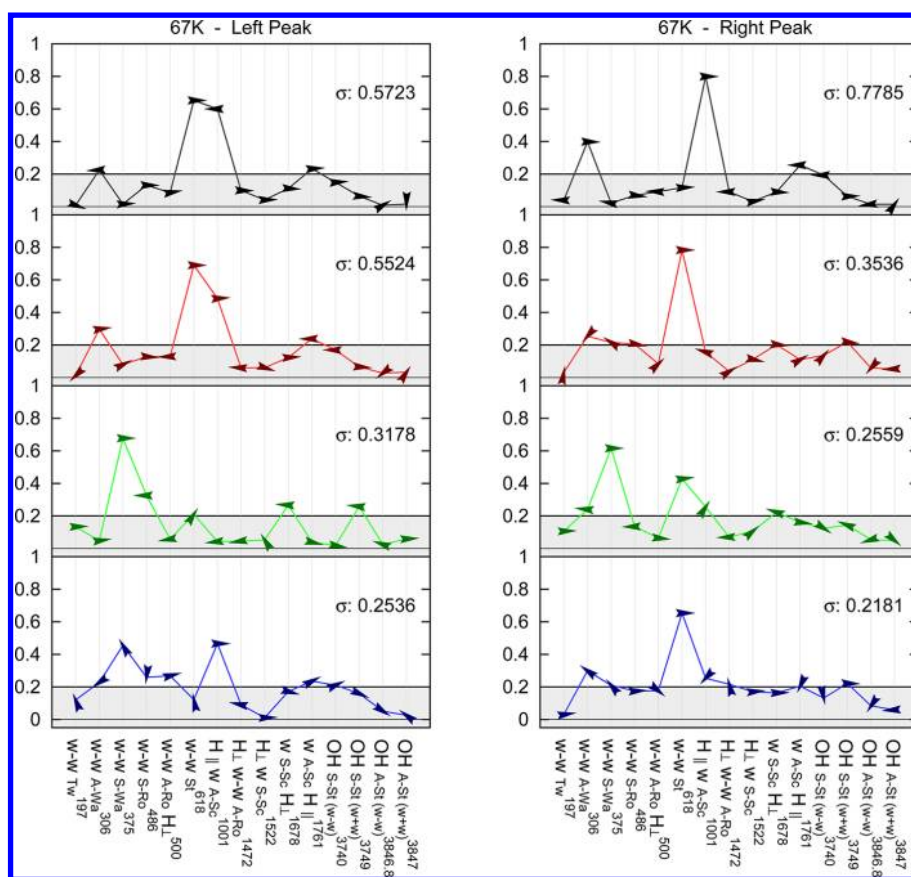


Figure 12. Harmonic normal mode components of SVD basis functions, $C_i^{\text{Harm}}[\vec{b}_i]$ in eq 24, for the 67 K doublet peaks. Arrows indicate the relative phase along coordinates associated with the fundamental harmonic in the Fourier series of \vec{b}_i . See eq 25.

entiating the two peaks, and to a lesser extent the water wag modes. This is qualitatively reminiscent of the conclusion in the fully quantum mechanical study by Vendrell et al.^{59–61} that the doublet can be seen to arise from a Fermi resonance between the proton transfer mode and a combined water–water stretch/asymmetric water wag mode. Of course, a precise correspondence is unclear given the difference in methodologies and corresponding definitions of zeroth order (or test) states.

The second approach taken here for the vibrational analysis of the doublet feature required no choice of zeroth order modes but rather considered (anharmonic) periodic vibrational motions projected from the dynamics, see section 2.2. The periodic projections corresponding to the frequency ranges of each peak were subsequently decomposed into relevant orthogonal vibrational basis functions using a singular value decomposition. It was found that two vibrational motions well represented as well as differentiated the motions of the two doublet peaks. Described qualitatively, these were the proton transfer and water–water stretch motions, both of which intrinsically carry water wag character. In the former analysis, the water wags were singled out in the results, a direct consequence of the particular reference modes (harmonic or Jacobi) chosen at the onset. The latter approach, however, identified the water wagging motion to be largely correlated to the proton transfer and water–water stretch, particularly in the lower temperature trajectories. As more of the lesser motions rise in prominence with increased temperature, the proton transfer and water–water stretch, that is, the symmetric and asymmetric shared proton stretches, remained most important.

The results presented here indicate that the Hamiltonian nonseparability with respect to, the symmetric and asymmetric shared proton stretches as the fundamental and differentiating characteristic motions within the frequency ranges of the doublet feature about 1000 cm^{-1} . As is apparent in Figures 4 and 6, the precise nature of the water–water stretch (asymmetric shared proton stretch) contribution to the lower frequency doublet peak is confused by the fact that the lower peak frequency range overlaps with the tail of a dark vibrational peak, primarily of asymmetric proton stretch character. In this aspect, further investigation merits additional measures, e.g., more frequency window functions, to isolate vibrations more directly linked to the features of interest in the dipole spectrum. Nevertheless, the ultimate importance of the asymmetric shared proton stretch in the doublet feature is affirmed in the singular value decompositions of the time translation symmetry projections over the spectral range of the higher frequency peak, where the second most significant basis functions are primarily water–water stretch vibrations. Further analysis is needed to understand the exact nature of the interaction between the symmetric and asymmetric shared proton stretching motions and implications on other Zundel-like systems.

■ ASSOCIATED CONTENT

Supporting Information

Graphical representations of the first four basis functions at each temperature. This material is available free of charge via the Internet at <http://pubs.acs.org>.

■ AUTHOR INFORMATION

Corresponding Author

*E-mail: iyengar@indiana.edu.

Notes

The authors declare no competing financial interest.

■ ACKNOWLEDGMENTS

This research was supported by the National Science Foundation, grant NSF CHE-1058949 to S.S.I. The authors are grateful to Professor Joel Bowman for providing a routine that computes the potential surface.

■ REFERENCES

- (1) Li, X.; Oomens, J.; Eyler, J. R.; Moore, D. T.; Iyengar, S. S. *J. Chem. Phys.* **2010**, *132*, 244301.
- (2) Li, X.; Moore, D. T.; Iyengar, S. S. *J. Chem. Phys.* **2008**, *128*, 184308.
- (3) Li, X.; Teige, V. E.; Iyengar, S. S. *J. Phys. Chem. A* **2007**, *111*, 4815–4820.
- (4) Iyengar, S. S. *J. Chem. Phys.* **2005**, *123*, 084310.
- (5) Iyengar, S. S. *J. Chem. Phys.* **2007**, *126*, 216101.
- (6) Iyengar, S. S.; Petersen, M. K.; Day, T. J. F.; Burnham, C. J.; Teige, V. E.; Voth, G. A. *J. Chem. Phys.* **2005**, *123*, 084309.
- (7) Iyengar, S. S.; Day, T. J. F.; Voth, G. A. *Int. J. Mass Spectrom.* **2005**, *241*, 197–204.
- (8) Dietrick, S. M.; Pacheco, A. B.; Phatak, P.; Stevens, P. S.; Iyengar, S. S. *J. Phys. Chem. A* **2012**, *116*, 399–414.
- (9) Pacheco, A. B.; Dietrick, S. M.; Stevens, P. S.; Iyengar, S. S. *J. Phys. Chem. A* **2012**, *116*, 4108.
- (10) Sumner, I.; Iyengar, S. S. *J. Phys. Chem. A* **2007**, *111*, 10313–10324.
- (11) Li, X.; Iyengar, S. S. *J. Chem. Phys.* **2010**, *133*, 184105.
- (12) Li, J.; Li, X.; Iyengar, S. S. *J. Chem. Phys.* Submitted.
- (13) Li, X.; Iyengar, S. S. *J. Phys. Chem. A* **2011**, *115*, 6269.
- (14) Iyengar, S. S.; Schlegel, H. B.; Millam, J. M.; Voth, G. A.; Scuseria, G. E.; Frisch, M. J. *J. Chem. Phys.* **2001**, *115*, 10291–10302.
- (15) Schlegel, H. B.; Iyengar, S. S.; Li, X.; Millam, J. M.; Voth, G. A.; Scuseria, G. E.; Frisch, M. J. *J. Chem. Phys.* **2002**, *117*, 8694–8704.
- (16) Rega, N.; Iyengar, S. S.; Voth, G. A.; Schlegel, H. B.; Vreven, T.; Frisch, M. J. *J. Phys. Chem. B* **2004**, *108*, 4210–4220.
- (17) Vimal, D.; Pacheco, A. B.; Iyengar, S. S.; Stevens, P. S. *J. Phys. Chem. A* **2008**, *112*, 7227–7237.
- (18) Diebold, G. J.; Engelke, F.; Lubman, D. M.; Whitehead, J. C.; Zare, R. N. *J. Chem. Phys.* **1977**, *67*, 5407.
- (19) Grant, E. R.; Coggiola, M. J.; Lee, Y. T.; Schulz, P. A.; Sudbo, A. S. *Chem. Phys. Lett.* **1977**, *52*, 595.
- (20) Bomse, D. S.; Woodin, R. L.; Beauchamp, J. L. *J. Am. Chem. Soc.* **1979**, *101*, 5503.
- (21) Valle, J. J.; Eyler, J. R.; Oomens, J.; Moore, D. T.; van der Meer, A. F. G.; von Helden, G.; Meijer, G.; Hendrickson, C. L.; Marshall, A. G.; Blakney, G. T. *Rev. Sci. Instrum.* **2005**, *76*.
- (22) Moore, D. T.; Oomens, J.; van der Meer, L.; von Helden, G.; Meijer, G.; Valle, J.; Marshall, A. G.; Eyler, J. R. *ChemPhysChem* **2004**, *5*, 740–743.
- (23) Fridgen, T. D.; MacAleese, L.; Maitre, P.; McMahon, T. B.; Boissel, P.; Lemaire, J. *Phys. Chem. Chem. Phys.* **2005**, *7*, 2747–2755.
- (24) Asmis, K. R.; Pivonka, N. L.; Santambrogio, G.; Brümmer, M.; Kaposta, C.; Neumark, D. M.; Wöste, L. *Science* **2003**, *299*, 1375.
- (25) Roscioli, J. R.; McCunn, L. R.; Johnson, M. A. *Science* **2007**, *316* (5822), 249–254.
- (26) Bowman, J. M. *Acc. Chem. Res.* **1986**, *19*, 202–208.
- (27) Gerber, R. B.; Ratner, M. A. *J. Chem. Phys.* **1988**, *70*, 97–132.
- (28) Jung, J. O.; Gerber, R. B. *J. Chem. Phys.* **1996**, *105*, 10332–10348.
- (29) Matsunaga, N.; Chaban, G. M.; Gerber, R. B. *J. Chem. Phys.* **2002**, *117*, 3541.
- (30) McCoy, A. B.; Gerber, R. B.; Ratner, M. A. *J. Chem. Phys.* **1994**, *101*, 1975.
- (31) McCoy, A. B.; Huang, X.; Carter, S.; Bowman, J. M. *J. Chem. Phys.* **2005**, *123*, 064317.
- (32) Iyengar, S. S.; Parker, G. A.; Kouri, D. J.; Hoffman, D. K. *J. Chem. Phys.* **1999**, *110*, 10283–10298.
- (33) Meyer, H.-D.; Manthe, U.; Cederbaum, L. S. *Chem. Phys. Lett.* **1990**, *165*, 73.
- (34) Althorpe, S. C.; Fernandez-Alonso, F.; Bean, B. D.; Ayers, J. D.; Pomerantz, A. E.; Zare, R. N.; Wrede, E. *Nature* **2002**, *416*, 67–70.
- (35) Huang, Y.; Iyengar, S. S.; Kouri, D. J.; Hoffman, D. K. *J. Chem. Phys.* **1996**, *105*, 927.
- (36) Makri, N. *Comput. Phys. Commun.* **1991**, *63*, 389–414.
- (37) Cao, J.; Voth, G. A. *J. Chem. Phys.* **1994**, *100*, 5106.
- (38) Deumens, E.; Diz, A.; Longo, R.; Öhrn, Y. *Rev. Mod. Phys.* **1994**, *66*, 917–983.
- (39) Hack, M. D.; Truhlar, D. G. *J. Phys. Chem. A* **2000**, *104*, 7917–7926.
- (40) Miller, W. H. *J. Phys. Chem. A* **2001**, *105*, 2942–2955.
- (41) Heller, E. J. *J. Chem. Phys.* **1975**, *62*, 1544–1555.
- (42) Hammes-Schiffer, S.; Tully, J. C. *J. Chem. Phys.* **1994**, *101*, 4657.
- (43) Ben-Nun, M.; Quenneville, J.; Martínez, T. J. *J. Phys. Chem. A* **2000**, *104*, 5161.
- (44) Micha, D. A. *J. Phys. Chem. A* **1999**, *103*, 7562–7574.
- (45) Gerber, R. B.; Buch, V.; Ratner, M. A. *J. Chem. Phys.* **1982**, *77*, 3022.
- (46) Bisseling, R. H.; Kosloff, R.; Gerber, R. B.; Ratner, M. A.; Gibson, L.; Cerjan, C. *J. Chem. Phys.* **1987**, *87*, 2760–2765.
- (47) Makri, N.; Miller, W. H. *J. Chem. Phys.* **1987**, *87*, 5781–5787.
- (48) Skone, J. H.; Pak, M. V.; Hammes-Schiffer, S. *J. Chem. Phys.* **2005**, *123*.
- (49) Swalina, C.; Hammes-Schiffer, S. *J. Phys. Chem. A* **2005**, *109*, 10410.
- (50) Lopez, J. G.; McCoy, A. B. *J. Phys. Chem. A* **2006**, *110*, 5450–5457.
- (51) Diken, E. G.; Headrick, J. M.; Roscioli, J. R.; Bopp, J. C.; Johnson, M. A.; McCoy, A. B.; Huang, X.; Carter, S.; Bowman, J. M. *J. Phys. Chem. A* **2005**, *109*, 571–575.
- (52) Hammer, N. I.; Diken, E. G.; Roscioli, J. R.; Johnson, M. A.; Myshakin, E. M.; Jordan, K. D.; McCoy, A. B.; Huang, X.; Bowman, J. M.; Carter, S. *J. Chem. Phys.* **2005**, *122* (24), 244301.
- (53) Headrick, J. M.; Diken, E. G.; Walters, R. S.; Hammer, N. I.; Christie, R. A.; Cui, J.; Myshakin, E. M.; Duncan, M. A.; Johnson, M. A.; Jordan, K. *Science* **2005**, *308*, 1765–1769.
- (54) Diken, E. G.; Headrick, J. M.; Roscioli, J. R.; Bopp, J. C.; Johnson, M. A.; McCoy, A. B. *J. Phys. Chem. A* **2005**, *109*, 1487–1490.
- (55) Fridgen, T. D.; McMahon, T. B.; MacAleese, L.; Lemaire, J.; Maitre, P. *J. Phys. Chem. A* **2004**, *108*, 9008.
- (56) Vener, M. V.; Kuhn, O.; Sauer, J. *J. Chem. Phys.* **2001**, *114*, 240.
- (57) Kaledin, M.; Kaledin, A. L.; Bowman, J. M. *J. Phys. Chem. A* **2006**, *110*, 2933.
- (58) Xie, Y.; Remington, R. B.; Schaefer, H. F., III. *J. Chem. Phys.* **1994**, *101*, 4878–4884.
- (59) Vendrell, O.; Gatti, F.; Meyer, H.-D. *Angew. Chem., Int. Ed.* **2007**, *46*, 6918.
- (60) Vendrell, O.; Gatti, F.; Meyer, H.-D. *J. Chem. Phys.* **2007**, *127*, 184303.
- (61) Vendrell, O.; Gatti, F.; Meyer, H.-D. *Angew. Chem., Int. Ed.* **2009**, *48*, 352.
- (62) Gordon, R. G. *Adv. Magn. Reson.* **1968**, *3*, 1.
- (63) McQuarrie, D. A. *Statistical Mechanics*; University Science Books: Sausalito, CA, 2000.
- (64) Berens, P. H.; White, S. R.; Wilson, K. R. *J. Chem. Phys.* **1981**, *75*, 515.
- (65) Bader, J. S.; Berne, B. J. *J. Chem. Phys.* **1994**, *100*, 8359.
- (66) Lawrence, C. P.; Nakayama, A.; Makri, N.; Skinner, J. L. *J. Chem. Phys.* **2004**, *120*, 6621.

- (67) Shin, J.-W.; Hammer, N. I.; Diken, E. G.; Johnson, M. A.; Walters, R. S.; Jaeger, T. D.; Duncan, M. A.; Christie, R. A.; Jordan, K. D. *Science* **2004**, *304*, 1137–1140.
- (68) Smith, F. T. *J. Chem. Phys.* **1959**, *31*, 1352.
- (69) Smith, F. T. *Phys. Rev.* **1960**, *120*, 1058.
- (70) Smith, F. T. *J. Math. Phys.* **1962**, *3*, 735.
- (71) Hirschfelder, J. O.; Dahler, J. S. *Proc. Natl. Acad. Sci. U. S. A.* **1956**, *42*, 363.
- (72) Golub, G. H.; Loan, C. F. V. *Matrix Computations*; The Johns Hopkins University Press: Baltimore, MD, 1996.
- (73) Zundel, G. *The Hydrogen Bond - Recent Developments in Theory and Experiments. II. Structure and Spectroscopy*; Schuster, P., Zundel, G., Sandorfy, C., Eds.; North-Holland: Amsterdam, 1976; pp 683–766.
- (74) Eigen, M. *Angew. Chem., Int. Ed. Engl.* **1964**, *3*, 1.
- (75) Cleland, W. W.; Kreevoy, M. M. *Science* **1994**, *264* (5167), 1887–1890.
- (76) Frey, P. A.; Whitt, S. A.; Tobin, J. B. *Science* **1994**, *264* (5167), 1927–1930.
- (77) Chatfield, D. C.; Brooks, B. R. *J. Am. Chem. Soc.* **1995**, *117*, 5561.
- (78) Warshel, A.; Papazyan, A.; Kollman, P. A. *Science* **1995**, *269*, 102.
- (79) Gerlt, J. A.; Kreevoy, M. M.; Cleland, W. W.; Frey, P. A. *Chem. Biol.* **1997**, *4*, 259.
- (80) Perrin, C. L.; Nielson, J. B. *Annu. Rev. Phys. Chem.* **1997**, *48*, 511–544.
- (81) Warshel, A.; Papazyan, A. *Proc. Natl. Acad. Sci. U. S. A.* **1996**, *93* (24), 13665–13670.
- (82) Harris, D. L. *J. Inorg. Biochem.* **2002**, *91* (4), 568–585.
- (83) Suhm, M. A.; Watts, R. O. *Phys. Rep.* **1991**, *204* (4), 293–329.
- (84) Anderson, J. B. *J. Chem. Phys.* **1975**, *63*, 1499–1503.
- (85) Bowman, J.; Carter, S.; Huang, X. *Int. Rev. Phys. Chem.* **2003**, *22*, 533.
- (86) Carter, S.; Culik, S. J.; Bowman, J. M. *J. Chem. Phys.* **1997**, *107*, 10458.
- (87) Carter, S.; Bowman, J. M.; Handy, N. C. *Theor. Chem. Acc.* **1998**, *100*, 191.
- (88) Carter, S.; Bowman, J. M. *J. Chem. Phys.* **1998**, *108*, 4397.
- (89) Carter, S.; Bowman, J. M. *J. Phys. Chem. A* **2000**, *104*, 2355.
- (90) Huang, X. C.; Braams, B. J.; Bowman, J. M. *J. Phys. Chem. A* **2006**, *110*, 445.
- (91) Beck, M. H.; Jackle, A.; Worth, G. A.; Meyer, H.-D. *Phys. Rep.* **2000**, *324*, 1.
- (92) Frisch, M. J.; Trucks, G. W.; Schlegel, H. B.; Scuseria, G. E.; Robb, M. A.; Cheeseman, J. R.; Montgomery, J. A., Jr.; Vreven, T.; Scalmani, G.; Kudin, K. N.; Iyengar, S. S.; Tomasi, J.; Barone, V.; Mennucci, B.; Cossi, M.; Rega, N.; Petersson, G. A.; Nakatsuji, H.; Hada, M.; Ehara, M.; Toyota, K.; Fukuda, R.; Hasegawa, J.; Ishida, M.; Nakajima, T.; Honda, Y.; Kitao, O.; Nakai, H.; Li, X.; Hratchian, H. P.; Peralta, J. E.; Izmaylov, A. F.; Brothers, E.; Staroverov, V.; Kobayashi, R.; Normand, J.; Burant, J. C.; Millam, J. M.; Klene, M.; Knox, J. E.; Cross, J. B.; Bakken, V.; Adamo, C.; Jaramillo, J.; Gomperts, R.; Stratmann, R. E.; Yazyev, O.; Austin, A. J.; Cammi, R.; Pomelli, C.; Ochterski, J. W.; Ayala, P. Y.; Morokuma, K.; Voth, G. A.; Salvador, P.; Dannenberg, J. J.; Zakrzewski, V. G.; Dapprich, S.; Daniels, A. D.; Strain, M. C.; Farkas, O.; Malick, D. K.; Rabuck, A. D.; Raghavachari, K.; Foresman, J. B.; Ortiz, J. V.; Cui, Q.; Baboul, A. G.; Clifford, S.; Cioslowski, J.; Stefanov, B. B.; Liu, G.; Liashenko, A.; Piskorz, P.; Komaromi, I.; Martin, R. L.; Fox, D. J.; Keith, T.; Al-Laham, M. A.; Peng, C. Y.; Nanayakkara, A.; Challacombe, M.; Chen, W.; Wong, M. W.; Pople, J. A. *Gaussian Development Version*, revision e.05; Gaussian, Inc.: Wallingford, CT, 2006.
- (93) Stoyanov, E. S.; Reed, C. A. *J. Phys. Chem. A* **2006**, *110* (48), 12992.